PCCP

PAPER

Cite this: *Phys. Chem. Chem. Phys.*, 2018, **20**, 16005

Water desalination using graphene nanopores: influence of the water models used in simulations†

Vishnu Prasad K.,*[a] Sridhar Kumar Kannam,[bc] Remco Hartkamp [d] and Sarith P. Sathian *[a]

Received 8th February 2018,
Accepted 21st May 2018

DOI: 10.1039/c8cp00919h

rsc.li/pccp

Molecular dynamics simulations are widely employed to analyze water and ion permeation through nanoporous membranes for reverse osmosis applications. In such simulations, water models play an important role in accurately reproducing the properties of water. We investigated the water and ion transport across a hydroxyl (OH) functionalized graphene nanopore using six water models: SPC, SPC/E, SPC/Fw, TIP3P, TIP4P, and TIP4P/2005. The water flux thus obtained varied up to 84% between the models. The water and ion flux showed a correlation with the bulk transport properties of the models such as the diffusion coefficient and shear viscosity. We found that the hydrogen-bond lifetime, resulting from the partial charges of the model, influenced the flux. Our results are useful in the selection of a water model for computer simulations of desalination using nanomembranes. Our findings also suggest that lowering the hydrogen-bond lifetime and enhancing the rate of diffusion of water would lead to enhanced water/ion flux.

1 Introduction

Reverse osmosis (RO), a membrane based separation technique, is a promising solution to the rising global demand for potable water. RO has a low energy requirement and low cost compared to other separation techniques such as multistage flash distillation, multi-effect distillation, membrane distillation *etc.*[1] Hence, it finds wide applications in wastewater treatment, pH neutralization, food and beverage processing, and separation of organic mixtures.[2] The performance of RO process depends on the water permeation rate and the ion filtration efficiency of the membrane.[3] Commercial RO plants employ metallic, ceramic, and polymer based materials as membranes whose performance is far from ideal.

Carbon-based nanomaterials, such as carbon nanotubes (CNTs),[4] graphene oxide membranes, and graphene nanopores,[5] show unparalleled water permeation rates owing to their inherent hydrophobicity.[6] Studies have indicated that graphene nanopores possess the potential to become a super membrane for RO desalination.[5,7–10] For example, Surwade *et al.*[11] have reported a water permeation of 5.96 L cm^{-2} day^{-1} MPa^{-1} through graphene nanopores with an ion selectivity of nearly 100%. Numerous studies have been conducted on desalination across nanopores using computational techniques such as molecular dynamics (MD). Cohen-Tanugi and Grossman reported two orders of magnitude higher water permeation through functionalized graphene nanopores compared to commercially used RO membranes, while maintaining the salt rejection efficiency.[12–14] Konatham *et al.*[15] studied interactions between the pore, water, and ions in functionalized graphene nanopores and elucidated the mechanisms involved in desalination. The authors reported a hydroxyl (OH) functionalized graphene nanopore as a suitable choice since this showed a low potential energy barrier for water and a high energy barrier for ions. Theoretical investigations using computer simulations on graphene nanopores have focused on water permeation,[16,17] ion transport,[18–20] the effect of pore geometry,[21,22] and functionalization,[23,24] aiming at maximum membrane performance.

The above studies, carried out using MD simulations, are based on inter-atomic interaction potentials and parameters (force-field), optimized to reproduce certain fluid or solid material properties. The properties of water are particularly interesting and challenging to reproduce, due to its numerous anomalies largely caused by its affinity to form hydrogen bonds. Various force fields, known as water models, have been developed in an attempt to accurately reproduce specific properties of water at various thermodynamic conditions.[25] However, quantities determined using different water models differ from each other since each model becomes successful in evaluating only a few properties of water accurately.[26] Hence, ambiguity exists in the results obtained from similar studies that used different water models. For example, a flux of 9 L cm^{-2} day^{-1} MPa^{-1} was found for a hydrogen

[a] *Department of Applied Mechanics, Indian Institute of Technology Madras, Chennai, India. E-mail: sarith@iitm.ac.in*
[b] *Faculty of Science, Engineering and Technology, Swinburne University of Technology, Melbourne, Victoria 3122, Australia*
[c] *School of Applied Sciences, RMIT University, Melbourne, Victoria 3001, Australia*
[d] *Process and Energy Department, Delft University of Technology, Leeghwaterstraat 39, 2628 CB Delft, The Netherlands*

† Electronic supplementary information (ESI) available. See DOI: 10.1039/c8cp00919h

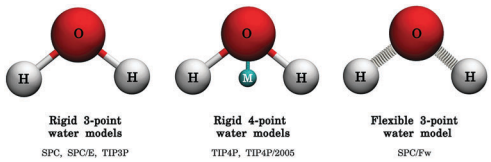

Fig. 1 Illustration of water models used in the present study.

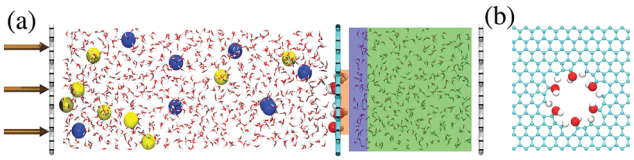

Fig. 2 (a) Snapshot of the simulated system. The graphene nanopore is represented by the central cyan sheet. The functional groups on the pore are shown by the red and white spheres representing oxygen and hydrogen. The water molecules are represented smaller for visibility. The sodium and chloride ions dispersed in the feed reservoir (0.5 M) are represented by the yellow and blue spheres. The ends of the feed reservoir (left) and the permeate reservoir (right) are provided with two graphene pistons represented by the silver sheets at the ends. Three regions, namely the pore, the interface (within 4.8 Å from the nanopore), and the bulk are illustrated using orange, blue, and green colors on the permeate side. The arrows indicate the direction in which a distributed force acted on the piston. (b) The front view of the nanopore.

passivated pore of 47 Å^2 using the SPC/E model,[23] while for a similar pore size, a much larger flux of 51 L cm^{-2} day^{-1} MPa^{-1} was found using the TIP4P model.[12] The latter studies are in line with another study, in which a flux of 40 L cm^{-2} day^{-1} MPa^{-1} was found for a pore of area 38.5 Å^2 using TIP4P/2005.[17] The above results do not confirm whether the pore size or the water model primarily influences the water flux. However, Liu and Patey[27] reported a considerable difference in the flux through CNTs (diameters 10.98 Å and 12.35 Å) using the TIP3P, TIP4P/2005, and SPC/E models, attributed to the difference in radial structures water forms inside the CNTs with different models. In a later study, the same authors reported similar observations for CNTs of 8.23 Å diameter with single-file flow.[28] The authors attributed the flux difference that resulted from different water models with single file flow through the CNTs to the activation energy of entry and the bulk transport properties of the models. Moreover, their recent study reported a dependence of ion transport across CNTs on the water model used.[29] These findings strongly indicate the apparent influence of water model on the water and ion transport across nanopores. Hence, selection of a suitable water model for investigating water desalination across nanopores would be an important step towards achieving consistent and reliable results.

Here, we determine the water and ion flux across graphene nanopores using the SPC,[30] SPC/E,[31] SPC/Fw,[32] TIP3P,[33] TIP4P,[34] and TIP4P/2005[35] models using non-equilibrium molecular dynamics (NEMD). Fig. 1 illustrates the water models used in this study. The models considered here are all rigid, with the exception of SPC/Fw. TIP4P and TIP4P/2005 are four-point models and all the others are three-point models. From the transport properties of water obtained using different water models, we explain the observed difference in the flux. Furthermore, utilizing equilibrium molecular dynamics (EMD), we analyze the hydrogen-bond dynamics and the potential energy barrier across the nanopore for water molecules. From the results obtained, we describe how the flux obtained is related to the bulk transport properties of water.

2 Methodology

We have simulated a graphene nanopore with six alternate hydroxyl (OH) and hydrogen (H) functionals with a pore area of 28 Å^2 [12] as shown in Fig. 2. Graphene sheets of dimensions 24.5 × 24.5 Å^2 were used. The feed reservoir was 60 Å long and filled with water (877 molecules) and ions corresponding to 0.5 M concentration (8 Na^+ and 8 Cl^-). The permeate reservoir was 30 Å long containing only water (395 molecules). Graphene sheets served as pistons at both ends of the reservoirs to maintain a pressure difference between both sides of the membrane as water permeates through the pore. Additional empty space was present beyond the pistons to prevent atoms from interacting across the periodic boundary.

Interaction parameters for ions, carbon and the functional groups from Cohen-Tanugi and Grossman[12] were used. Water was modeled using the parameters of the respective water models. We used a cut-off of 12.0 Å for the Lennard-Jones (LJ)[36] potentials and the short-range electrostatic interactions. The coulombic forces were corrected to account for long-range interactions using the particle–particle–particle mesh (PPPM)[37] method, with a relative root mean square error in per-atom force calculations below 1 × 10^{-6}. Periodic boundary conditions were applied in all directions. Both the pistons and the pore graphene sheet were kept rigid. Except for SPC/Fw, the O–H bonds and H–O–H angles were kept rigid using the SHAKE[38] algorithm. Simulations were carried out using the large atomic/molecular massively parallel simulator (LAMMPS)[39] package. A timestep of 1 fs was used for the simulations.

First, an optimal configuration for the functional groups on the pore rim was obtained using energy minimization, keeping the sheets, the water and the ions rigid. Then, keeping the functional groups and the sheets rigid, the energy of the entire system was minimized. Throughout the simulation, the pore sheet atoms were kept rigid and an axial force was applied on the pistons after removing the lateral forces on them to ensure their rigidity. The water and ions were then equilibrated at 300 K temperature using a Nosé–Hoover thermostat.[40] After monitoring the potential energy of the system, an equilibration time of 1 ns was used. An external force (equal to the product of the requisite pressure and the area of a piston sheet divided by the number of atoms constituting the piston sheet) was imposed on atoms of both pistons in opposite directions to create 0.101325 MPa (1 atm) pressure in the feed and permeate reservoirs. After equilibration, during the production run, the feed side piston was provided with an additional force to generate a pressure of 200 MPa in the feed reservoir, while maintaining 0.101325 MPa (1 atm) pressure in the permeate side. This applied pressure gradient is two orders of magnitude

higher than that of experiments, but was necessary to achieve a measurable flux within the simulation run time. The production run was carried out for 5 ns (until the feed side reservoir was almost drained) for all the runs and the flux was monitored every 100 fs to ensure sufficient statistics. Five independent simulations with different initial velocities were performed for each model to gather sufficient statistics.

EMD simulations coupled with the adaptive biasing forcing (ABF) algorithm[41,42] were used to determine the energy barrier across the nanopore. Here, the reaction coordinate (the same as the pore axis or z-axis) is divided into M equally sized bins of width δz. The mean force on the water molecules in the kth bin along the z-axis is evaluated using the equation.[43]

$$\bar{F}_z(N_{\text{step}}, k) = \frac{1}{N^k_{\text{step}}} \sum_{\mu=1}^{N^k_{\text{step}}} F^k_\mu \quad (1)$$

where N_{step} indicates the current time step. This force is used to continuously bias the simulation to sample all the bins. Also, after acquiring sufficient statistics in each bin, the force is integrated along the reaction coordinate to obtain the potential of mean force (PMF).[43]

$$\Delta A_z = -\sum_{i=1}^{M} \bar{F}_z(N_{\text{step}}, k)\delta z \quad (2)$$

A length of 10 Å along the pore axis, preceding the pore, was sampled for 20 ns with a timestep of 1 fs. The colvars module for LAMMPS[44] was used for the PMF calculations. EMD simulations were also carried out to investigate the hydrogen-bond dynamics. The trajectories were recorded at every fs to evaluate the hydrogen-bond time autocorrelation function which typically decays within 10 ps. The analysis was carried out in three predefined regions, namely pore, interface, and bulk (see Fig. 2). The pore region is defined to calculate the hydrogen-bond dynamics between the water molecules and the functional groups on the pore rim. The interface region spans from the nanopore to the first minimum after the first maximum in the density profile (see Fig. 6), that is, within 4.8 Å from the graphene sheet. The remaining region is considered as the bulk region. Furthermore, EMD simulations were conducted using a periodic water box of 268 water molecules to calculate the diffusion coefficient. The system was equilibrated at 300 K and 0.101325 MPa (1 atm) for 1 ns and was then maintained at constant volume and temperature for 1 ns, during which the trajectories were recorded every 10 fs. The diffusion coefficient was then calculated from 5 sample simulations, each of length 200 ps, using the equation given below.

$$D = \frac{1}{2N_{\text{D}}\tau(t_{\text{L}} - t_{\text{F}} - \tau)} \sum_{t_0=t_{\text{F}}}^{t_0=t_{\text{L}}-\tau} \frac{1}{N} \sum_{i=1}^{i=N} (r_i(t_0+\tau) - r_i(t_0))^2 \quad (3)$$

where, N_{D} represents the number of dimensions of the system (here, N_{D} = 3), τ is the time interval, t_{F} and t_{L} are the times corresponding to the first (0 ps) and last (200 ps) snapshots of the trajectory, respectively, N is the number of water molecules, and $r_i(t)$ is the position vector of the ith water molecule at time t. The limiting diffusion coefficient at τ = 50 ps obtained from sample simulations was used to obtain the average diffusion coefficient and the error estimates.

3 Results and discussion

Fig. 3(a) shows the running average of the velocity (V) of water along the flow direction (z), with time (t). Fig. 3(b) shows the number of water molecules (N_{w}) crossing the membrane with time (t). The slope of N_{w} in Fig. 3(b) is the water flux (Q_{w}).

The highest measured flux, shown by the TIP3P model, was 84% greater than the lowest measured flux shown by TIP4P/2005. In general, the use of three-point water models resulted in higher fluxes compared to the four-point models, with the exception of SPC/E which showed a flux close to that of TIP4P. SPC/E[31] reproduces the properties of water with an accuracy similar to the four-point water models. It also emulates the structural characteristics of ice similar to TIP4P.[26,45] This could be the reason for the low flux shown by SPC/E. The succession of water models according to their flux magnitudes agrees with that reported for CNTs.[28]

We found that the properties of water are strongly affected by the partial charges on the atoms in the water model. For example, the SPC/E and SPC models showed a 34% difference in the flux, even though they only differ in their partial charges. Also, SPC/E has larger partial charge magnitudes than SPC, resulting in stronger electrostatic correlations between the molecules and solvation of ions, explaining the lower flux of this model. Similarly, the TIP3P and TIP4P models differ in their partial charge distribution and showed a 50% difference in the flux even though they had the same geometry and similar LJ parameters. Furthermore, the SPC and TIP3P models, having similar partial charges, produced similar fluxes. These observations indicate that the partial charges grossly influence the water flux across the nanopore.

The TIP4P and TIP4P/2005 models differ in their partial charges and LJ parameters, but have the same bond length and angle. They showed a 20% difference in the flux. From the results

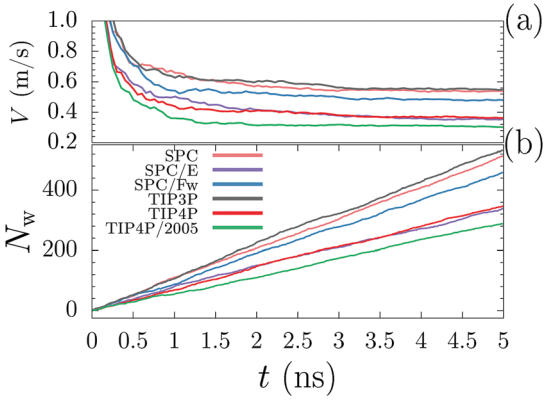

Fig. 3 (a) The running average of the velocity of water molecules along the flow direction (along the z axis, which is same as the pore axis) with time. (b) Flux is defined as the number of water molecules crossing the pore with time. The results are averaged over five independent simulations with a pressure difference of 200 MPa at 300 K temperature.

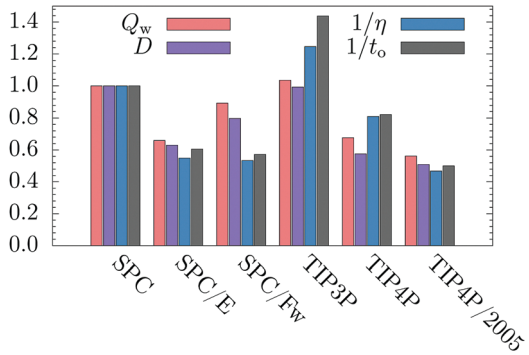

Fig. 4 Correlation between the flux, diffusion coefficient, shear viscosity, and orientational relaxation time. The values are normalized with respect to SPC model values. The shear viscosity and orientational relaxation time are inverted to illustrate the correlation better.

for the three-point models, we assume this to have resulted from their difference in partial charges. However, the SPC/Fw model showed a lower flux than SPC, even when both have the same charges. We assume this to have resulted from the difference in bond and angle length of SPC/Fw and due to the model's flexibility.

Fig. 4 shows the flux (Q_w) obtained and the bulk diffusion coefficient (D) determined in the present study. The bulk properties of water such as shear viscosity (η) and orientational relaxation time (t_o), found using different water models, are also shown.[26,32] All the values are normalized with respect to SPC values for the ease of comparing data with different orders of magnitude. Table 1 shows the data corresponding to Fig. 4. The results show a direct correlation between the diffusion coefficient and the flux, indicating that the flux depends on the degree of activity of the simulated water. The inverted shear viscosity and orientational relaxation time also showed a similar trend. The results agree with previous studies on CNTs.[28,29] If we assume a continuum, the shear viscosity and diffusion coefficient are inversely related, as per the Stokes–Einstein relationship. Therefore, the direct correlation of flux and diffusion coefficient implies their inverse correlation with the shear viscosity. However, the correlation shown by the flux and the property values is not strict. For example, the flux shown by TIP4P is higher than SPC/E even though TIP4P has a lower diffusion coefficient. Similar disparity was also shown by SPC and TIP3P.

To further improve our understanding of the relation between the transport properties and the flux obtained using the water models, the hydrogen-bond dynamics was analyzed. Here, two water molecules were considered to be hydrogen bonded if the oxygen atoms were within 3.5 Å of each other and the oxygen–hydrogen–oxygen angle exceeded 140°.[46] The hydrogen-bond lifetime of water, τ, was measured using the time autocorrelation function,[47,48] given as,

$$C_c(t) = \left\langle \frac{\sum h_{ij}(t_0)h_{ij}(t_0+t)}{\sum h_{ij}(t_0)^2} \right\rangle_{ij} \quad (4)$$

where "ij" represents any random pair of donor and acceptor. $h_{ij}(t)$ would either be 0 or 1 depending on whether the donor–acceptor pair "i" and "j" are hydrogen bonded at time t. $h_{ij}(t)$ takes the value 1 if the hydrogen bond between "i" and "j" is intact during time t, otherwise it is 0.[48] The subscript "c" in $C_c(t)$ represents the continuous definition of the time autocorrelation function, by which a hydrogen bond once broken is considered broken in all the succeeding instants.[47,48] Eqn (5) was fit to the hydrogen-bond decay (see Fig. 5(a)).

$$C_{fit}(t) \approx A_1 e^{t/\tau_1} + (1 - A_1)e^{t/\tau_2} \quad (5)$$

where A_1, τ_1 and τ_2, are fitting parameters. The average values obtained for A_1, τ_1 and τ_2 are provided in ESI† (see Table S1). The hydrogen-bond lifetime, τ, for the pore, the interface, and the bulk region was found by integrating eqn (5).[47]

$$\text{Hydrogen-bond lifetime, } \tau = \int_0^\infty C_{fit}(t) \quad (6)$$

Hydrogen-bond lifetime and the average number of hydrogen bonds per water molecule were measured for the pore, the interface, and the bulk regions (see the methodology section).

Table 2 shows the number of hydrogen bonds per water molecule and the hydrogen-bond lifetime for the three regions. The number of hydrogen bonds per molecule obtained for the bulk region is similar to the previous study.[49] The number of hydrogen bonds per molecule in the interface region is less than that in the bulk region.[46,50] Also, the pore region has the least number of hydrogen bonds since the number of molecules involved here was the least. In each region, the number of

Table 1 The flux (Q_w, ns^{-1}), diffusion coefficient (D, 10^{-5} cm^2 s^{-1}), shear viscosity (η, mPa s), and orientational relaxation time (t_o, ps) of water models. The flux and diffusion coefficient are measured in the present study. Values in parenthesis provide the standard error. The shear viscosity and orientational relaxation time for SPC and SPC/Fw were taken from Wu *et al.*[32] (1.013 bar, 298.15 K). Values corresponding to the other water models, and the experimental values, were taken from Vega and Abascal[26] (1 bar, 298 K)

Water model	Q_w	D	η	t_o
SPC	102.72 (2.72)	4.05 (0.04)	0.40	1.15
SPC/E	67.72 (2.36)	2.55 (0.02)	0.72	1.90
SPC/Fw	91.80 (2.77)	3.23 (0.04)	0.75	2.01
TIP3P	106.36 (3.46)	4.02 (0.03)	0.32	0.80
TIP4P	69.52 (2.68)	2.33 (0.04)	0.49	1.40
TIP4P/2005	57.72 (2.87)	2.06 (0.03)	0.85	2.30
Experimental value	NA	2.30	0.89	2.36

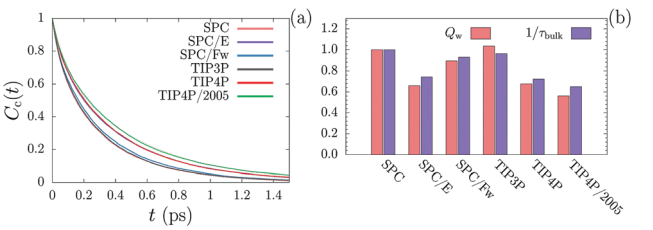

Fig. 5 (a) Hydrogen-bond time autocorrelation function (see eqn (4)) for water in the bulk region. Dotted lines represent the fitting curves. (b) Correlation between the hydrogen-bond lifetime and the flux. The values are normalized with respect to SPC values. The hydrogen-bond lifetime is inverted to illustrate the correlation better.

Table 2 The average number of hydrogen bonds per water molecule and the hydrogen-bond lifetime. Three predefined regions, namely pore, interface, and bulk (see the Methodology section), were analyzed. Estimates from hydrogen bonding within water are labeled as W–W and those between water and the pore functionals are labeled as W–P. The hydrogen-bond lifetime is expressed in ps. Values in parenthesis indicate the standard deviation

	Number of hydrogen bonds per water			Hydrogen-bond lifetime		
Water model	W–W (bulk)	W–W (interface)	W–P (pore)	W–W (bulk) (τ_{bulk})	W–W (interface) ($\tau_{interface}$)	W–P (pore) (τ_{pore})
SPC	3.06 (0.03)	2.29 (0.09)	1.14 (0.35)	0.26 (0.00)	0.23 (0.02)	0.21 (0.08)
SPC/E	3.19 (0.03)	2.42 (0.09)	1.13 (0.34)	0.35 (0.00)	0.27 (0.03)	0.26 (0.11)
SPC/Fw	3.12 (0.03)	2.33 (0.09)	1.09 (0.29)	0.28 (0.00)	0.22 (0.02)	0.19 (0.08)
TIP3P	3.07 (0.03)	2.30 (0.09)	1.19 (0.40)	0.27 (0.01)	0.23 (0.02)	0.21 (0.08)
TIP4P	3.24 (0.03)	2.45 (0.08)	1.10 (0.30)	0.36 (0.01)	0.28 (0.03)	0.28 (0.14)
TIP4P/2005	3.29 (0.03)	2.43 (0.08)	1.08 (0.27)	0.40 (0.01)	0.30 (0.03)	0.36 (0.20)

hydrogen bonds was similar for each model.[51] The results are confirmed by analyzing the number of hydrogen bonds per molecule along the pore axis (see Fig. S1 in ESI†).[52] It has been reported that the distribution of neighboring molecules in water, simulated using different water models, varies minimally.[53] As a result, the numbers of hydrogen bonds per molecule for different models in each region were similar. This indicates that the flux is minimally influenced by the number of hydrogen bonds that water makes per molecule.

Fig. 5(a) shows the hydrogen-bond time autocorrelation function, $C_c(t)$ (eqn (4)), for the water in the bulk region.[54] The dotted lines represent the fitting curves. Fig. 5(b) shows the correlation between the hydrogen-bond lifetime (τ_{bulk}) and the flux (Q_w). As shown in Fig. 5(b), the flux and the hydrogen-bond lifetime of water in the bulk region correlate inversely with each other. Analogous to this, Liu and Patey[27] have reported an inverse relation between the percentage of water making hydrogen bonded structures inside the CNTs and the resulting flux. The hydrogen-bond lifetimes of water in the interface and the pore region also show correlation with the flux (see Table 2), but are less conforming than the lifetime of the bulk region. The above observations were also found to be true for hydrogen passivated nanopores and also for different LJ potential and electrostatic cutoff values (see Fig. S2–S5 in ESI†).

From the above results, we deduce that the partial charges of the models grossly influence the hydrogen-bond dynamics, which in turn determine the rate of diffusion of water: the longer the hydrogen-bond lifetime, the lower the rate of diffusion. The difference in diffusion rates translates into the different flux values of different models during desalination. This signifies the important relationship between the partial charges and the flux mentioned earlier. Also, the above explanation reveals the relation between the hydrogen-bond lifetime, the diffusion coefficient, and the flux. However, the exact mechanism through which the partial charges of water influence its transport properties and the resultant flux is beyond the scope of this paper.

As a corollary, we infer that the water should have a lower hydrogen-bond lifetime[29] for a higher flux across the nanopore. Hence, breaking the hydrogen bonds more often[55,56] and enhancing the diffusion coefficient[57,58] would enhance the flux across the nanopore.

We determined the potential energy landscape for water molecules across the nanopore for different models, shown in Fig. 6(a). The PMF was evaluated along the flow direction

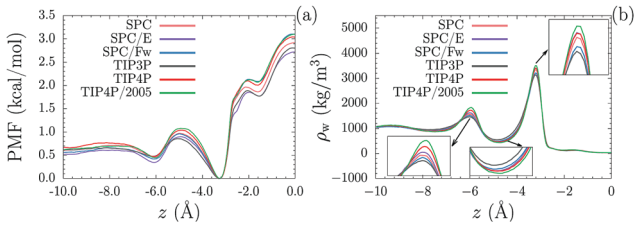

Fig. 6 (a) Potential of mean force of water molecules along the pore axis. (b) Density distribution of the water adjacent to the nanopore. The pore is located at z = 0.

(z-axis) using EMD simulations coupled to the ABF algorithm (see the Methodology section). The PMF profiles agree qualitatively with the previous study.[15] Except for the SPC/Fw and SPC/E models, the energy barrier showed an inverse relationship with respect to the measured flux. However, the PMF profile differed by less than 0.4 kcal mol^{-1} between the water models, which could be a consequence of the similar number of hydrogen bonds per molecule shown by the models. As PMF represents the molecular energy arising from the hydrogen bond formation and the distribution of neighboring molecules, a similar number of hydrogen bonds per molecule resulted in similar PMF profiles for each model considered.

Furthermore, Fig. 6(b) provides the density profile of water (ρ_w) along the pore axis (z-axis). There was minimal variation in the density profile among the different models, in agreement with the PMF profile. Also, the locations of maxima and minima in the density profile were inverse with respect to those in the PMF profile.[15] Fig. 6(b) shows two maxima within 10 Å from the nanopore, beyond which, the density approximates to the bulk density ($\sim$1000 kg m^{-3}). These results agree with previous studies.[16,46,50] Also, the magnitude of maxima and minima varied with the water model: the lower the flux shown by the model, the higher the maxima and the lower the minima.

Fig. 7(a) shows the correlation between the ion flux (Q_i) and the water flux (Q_w) across the nanopore. The results are again in good agreement with a recent study on CNTs.[29] Both water permeation and ion exclusion are equally important for desalination. However, the results indicate that enhancement in water flux by improving the diffusion coefficient would also result in enhanced ion seepage. Hence, whenever there is an improvement in the diffusion coefficient, the same should go

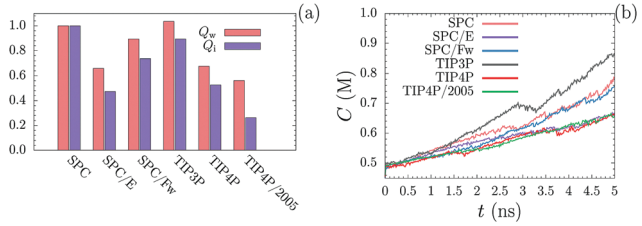

Fig. 7 (a) Comparison between the ion flux and the water flux. The ion flux comprises both anion and cation flux. The values are normalized with respect to SPC values. (b) The ion concentration in the feed reservoir with time.

together with appropriate ion exclusion methods for effective desalination.

Fig. 7(b) shows the feed side ion concentration (C) with time (t). The feed side ion concentration increased at varying rates depending on the model's flux: the higher the flux, the more rapid the concentration increase. In models with high water flux, the ion flux was also higher (from Fig. 7(a)). However, such models showed a very rapid increase in the feed side ion concentration. The result indicate the strong dependence of ion concentration on the water model used in desalination studies.

4 Conclusions

We investigated the dependence of the simulated water and ion flux across a hydroxyl functionalized graphene nanopore on the water model used. We considered the SPC, SPC/E, SPC/Fw, TIP3P, TIP4P, and TIP4P/2005 models for the study. The water flux varied up to 84% among the models. The partial charges, the hydrogen-bond dynamics, and the diffusion coefficient of the model are found to influence the flux. The flux was found to be directly proportional to the bulk properties of the simulated water such as the diffusion coefficient and the shear viscosity, and inversely proportional to the hydrogen-bond lifetime. We explained a possible mechanism that relates the partial charges, the diffusion coefficient and the flux obtained. The models showed a similar number of hydrogen bonds per molecule and a similar free energy profile for water along the pore axis. Furthermore, we observed a direct correlation between the ion flux and the water flux.

Our results indicate that water models that reproduce the transport properties and the hydrogen-bond dynamics of water to the best accuracy should be used for simulating desalination across nanopores. Among the rigid four-point models, TIP4P/2005 reproduces the diffusion coefficient and the shear viscosity of water close to the experimental values.[26,59] Hence, we suggest the use of the TIP4P/2005 model for computational studies on desalination across nanoporous membranes. Also, among the rigid three-point water models, SPC/E reproduces the hydrogen-bond dynamics to the best accuracy under confinement.[54] However, the diffusion coefficient and the shear viscosity produced by SPC/E are less accurate than those produced by TIP4P/2005.[26] These results can be extended to the study of permeability in other systems such as lipid membranes.[60] The results also indicate that a faster breakage of the hydrogen bonds and enhancement of the diffusion coefficient enhance the flux. However, this would also lead to a higher ion seepage, which needs to be checked using appropriate methods for effective desalination.

Conflicts of interest

There are no conflicts to declare.

Acknowledgements

We thank the financial support received from Department of Science and Technology (DST), Government of India, under Water Technology Initiative (Project Number: DST/TM/WTI/2K15/84(G)). We thank David Cohen-Tanugi, EMBR labs, Cambridge, USA, for sharing with us the nanopore geometry and other details for this study.

References

1 M. W. Shahzad, M. Burhan, L. Ang and K. C. Ng, *Desalination*, 2017, **413**, 52–64.
2 I. Wenten and Khoiruddin, *Desalination*, 2016, **391**, 112–125.
3 J. R. Werber, A. Deshmukh and M. Elimelech, *Environ. Sci. Technol. Lett.*, 2016, **3**, 112–120.
4 R. Das, M. E. Ali, S. B. A. Hamid, S. Ramakrishna and Z. Z. Chowdhury, *Desalination*, 2014, **336**, 97–109.
5 K. A. Mahmoud, B. Mansoor, A. Mansour and M. Khraisheh, *Desalination*, 2015, **356**, 208–225.
6 M. Hu, S. Zheng and B. Mi, *Environ. Sci. Technol.*, 2016, **50**, 685–693.
7 P. Goh and A. Ismail, *Desalination*, 2015, **356**, 115–128.
8 H. Ebro, Y. M. Kim and J. H. Kim, *J. Membr. Sci.*, 2013, **438**, 112–125.
9 D. Cohen-Tanugi and J. C. Grossman, *Desalination*, 2015, **366**, 59–70.
10 E. A. Müller, *Curr. Opin. Chem. Eng.*, 2013, **2**, 223–228.
11 S. P. Surwade, S. N. Smirnov, I. V. Vlassiouk, R. R. Unocic, G. M. Veith, S. Dai and S. M. Mahurin, *Nat. Nanotechnol.*, 2015, **10**, 459–464.
12 D. Cohen-Tanugi and J. C. Grossman, *Nano Lett.*, 2012, **12**, 3602–3608.
13 D. Cohen-Tanugi and J. C. Grossman, *J. Chem. Phys.*, 2014, **141**, 074704.
14 D. Cohen-Tanugi, R. K. McGovern, S. H. Dave, J. H. Lienhard and J. C. Grossman, *Energy Environ. Sci.*, 2014, **7**, 1134–1141.
15 D. Konatham, J. Yu, T. A. Ho and A. Striolo, *Langmuir*, 2013, **29**, 11884–11897.
16 M. E. Suk and N. R. Aluru, *RSC Adv.*, 2013, **3**, 9365.
17 L. Garnier, A. Szymczyk, P. Malfreyt and A. Ghoufi, *J. Phys. Chem. Lett.*, 2016, **7**, 3371–3376.
18 K. Sint, B. Wang and P. Král, *J. Am. Chem. Soc.*, 2008, **130**, 16448–16449.
19 M. E. Suk and N. R. Aluru, *J. Chem. Phys.*, 2014, **140**, 084707.

20 G. Hu, M. Mao and S. Ghosal, *Nanotechnology*, 2012, **23**, 395501.
21 M. Shahbabaei, D. Tang and D. Kim, *Comput. Mater. Sci.*, 2017, **128**, 87–97.
22 S. Gravelle, L. Joly, F. Detcheverry, C. Ybert, C. Cottin-Bizonne and L. Bocquet, *Proc. Natl. Acad. Sci. U. S. A.*, 2013, **110**, 16367–16372.
23 Q. Chen and X. Yang, *J. Membr. Sci.*, 2015, **496**, 108–117.
24 Y. Wang, Z. He, K. M. Gupta, Q. Shi and R. Lu, *Carbon*, 2017, **116**, 120–127.
25 S. Chakraborty, H. Kumar, C. Dasgupta and P. K. Maiti, *Acc. Chem. Res.*, 2017, **50**, 2139–2146.
26 C. Vega and J. L. F. Abascal, *Phys. Chem. Chem. Phys.*, 2011, **13**, 19663.
27 L. Liu and G. N. Patey, *J. Chem. Phys.*, 2014, **141**, 18C518.
28 L. Liu and G. N. Patey, *J. Chem. Phys.*, 2016, **144**, 184502.
29 L. Liu and G. N. Patey, *J. Chem. Phys.*, 2017, **146**, 074502.
30 H. J. C. Berendsen, J. P. M. Postma, W. F. van Gunsteren and J. Hermans, *The Jerusalem Symposia on Quantum Chemistry and Biochemistry*, Springer Nature, 1981, pp. 331–342.
31 H. J. C. Berendsen, J. R. Grigera and T. P. Straatsma, *J. Phys. Chem.*, 1987, **91**, 6269–6271.
32 Y. Wu, H. L. Tepper and G. A. Voth, *J. Chem. Phys.*, 2006, **124**, 024503.
33 D. J. Price and C. L. Brooks, *J. Chem. Phys.*, 2004, **121**, 10096–10103.
34 W. L. Jorgensen, J. Chandrasekhar, J. D. Madura, R. W. Impey and M. L. Klein, *J. Chem. Phys.*, 1983, **79**, 926–935.
35 J. L. F. Abascal and C. Vega, *J. Chem. Phys.*, 2005, **123**, 234505.
36 J. E. Lennard-Jones, *Proc. Phys. Soc.*, 1931, **43**, 461.
37 R. W. Hockney and J. W. Eastwood, *Computer simulation using particles*, CRS Press, 1988.
38 J.-P. Ryckaert, G. Ciccotti and H. J. Berendsen, *J. Comp. Physiol.*, 1977, **23**, 327–341.
39 S. Plimpton, *J. Comput. Phys.*, 1995, **117**, 1–19.
40 D. J. Evans and B. L. Holian, *J. Chem. Phys.*, 1985, **83**, 4069–4074.
41 E. Darve, D. Rodríguez-Gómez and A. Pohorille, *J. Chem. Phys.*, 2008, **128**, 144120.
42 J. Hénin, G. Fiorin, C. Chipot and M. L. Klein, *J. Chem. Theory Comput.*, 2010, **6**, 35–47.
43 J. Comer, J. C. Gumbart, J. Hénin, T. Lelièvre, A. Pohorille and C. Chipot, *J. Phys. Chem. B*, 2015, **119**, 1129–1151.
44 G. Fiorin, M. L. Klein and J. Hénin, *J. Mol. Phys.*, 2013, **111**, 3345–3362.
45 C. Vega, C. McBride, E. Sanz and J. L. F. Abascal, *Phys. Chem. Chem. Phys.*, 2005, **7**, 1450.
46 G. Cicero, J. C. Grossman, E. Schwegler, F. Gygi and G. Galli, *J. Am. Chem. Soc.*, 2008, **130**, 1871–1878.
47 R. J. Gowers and P. Carbone, *J. Chem. Phys.*, 2015, **142**, 224907.
48 D. Rapaport, *Mol. Phys.*, 1983, **50**, 1151–1162.
49 R. Hartkamp and B. Coasne, *J. Chem. Phys.*, 2014, **141**, 124508.
50 T. A. Ho and A. Striolo, *Mol. Simul.*, 2014, **40**, 1190–1200.
51 J. Zielkiewicz, *J. Chem. Phys.*, 2005, **123**, 104501.
52 A. M. Prpich, Y. Sheng, W. Wang, M. E. Biswas and P. Chen, *PLoS One*, 2009, **4**, e8281.
53 P. Mark and L. Nilsson, *J. Phys. Chem. A*, 2001, **105**, 9954–9960.
54 H. Kumar, C. Dasgupta and P. K. Maiti, *RSC Adv.*, 2015, **5**, 1893–1901.
55 Z. Wang, Y. Pang and D. D. Dlott, *J. Phys. Chem. A*, 2007, **111**, 3196–3208.
56 H. Ohtaki, *J. Mol. Liq.*, 2003, **103**, 3–13.
57 K. Krynicki, C. D. Green and D. W. Sawyer, *Faraday Discuss. Chem. Soc.*, 1978, **66**, 199–208.
58 K. R. Harris and L. A. Woolf, *J. Chem. Soc., Faraday Trans. 1*, 1980, **76**, 377.
59 A. P. Markesteijn, R. Hartkamp, S. Luding and J. Westerweel, *J. Chem. Phys.*, 2012, **136**, 134104.
60 R. Hartkamp, T. C. Moore, C. R. Iacovella, M. A. Thompson, P. A. Bulsara, D. J. Moore and C. McCabe, *J. Phys. Chem. B*, 2018, **122**, 3113–3123.